

May 16, 2017

Conformational Heterogeneity and FRET Data Interpretation for Dimensions of Unfolded Proteins

Jianhui SONG,^{1,2} Gregory-Neal GOMES,³
Tongfei SHI,⁴ Claudiu C. GRADINARU,³ and Hue Sun CHAN^{2,*}

¹ School of Polymer Science and Engineering, Qingdao University of Science and Technology, 53 Zhengzhou Road, Qingdao 266042, China;

² Departments of Biochemistry and Molecular Genetics, University of Toronto, Toronto, Ontario M5S 1A8, Canada;

³ Department of Chemical and Physical Sciences, University of Toronto Mississauga, Mississauga, Ontario L5L 1C6 Canada; and Department of Physics, University of Toronto, Toronto, Ontario M5S 1A7, Canada;

⁴ State Key Laboratory of Polymer Physics and Chemistry, Changchun Institute of Applied Chemistry, Chinese Academy of Sciences, Changchun 130022, China

* Corresponding author.

Hue Sun Chan. E-mail: chan@arrhenius.med.toronto.edu

Abstract

A mathematically valid formulation is required to infer properties of disordered protein conformations from single-molecule Förster resonance energy transfer (smFRET). Conformational dimensions inferred by conventional approaches that presume a homogeneous conformational ensemble can be unphysical. When all possible—heterogeneous as well as homogeneous—conformational distributions are taken into account without pre-judgement, a single value of average transfer efficiency $\langle E \rangle$ between dyes at two chain ends is generally consistent with highly diverse, multiple values of the average radius of gyration $\langle R_g \rangle$. Here we utilize unbiased conformational statistics from a coarse-grained explicit-chain model to establish a general logical framework to quantify this fundamental ambiguity in smFRET inference. As an application, we address the long-standing controversy regarding the denaturant dependence of $\langle R_g \rangle$ of unfolded proteins, focusing on Protein L as an example. Conventional smFRET inference concluded that $\langle R_g \rangle$ of unfolded Protein L is highly sensitive to [GuHCl], but data from small-angle X-ray scattering (SAXS) suggested a near-constant $\langle R_g \rangle$ irrespective of [GuHCl]. Strikingly, the present analysis indicates that although the reported $\langle E \rangle$ values for Protein L at [GuHCl] = 1 M and 7 M are very different at 0.75 and 0.45, respectively, the R_g^2 distributions consistent with these two $\langle E \rangle$ values overlap by as much as 75%. Our findings suggest, in general, that the smFRET-SAXS discrepancy regarding unfolded protein dimensions likely arise from highly heterogeneous conformational ensembles at low or zero denaturant, and that additional experimental probes will be needed to ascertain the nature of this heterogeneity.

Introduction

Single-molecule Förster resonance energy transfer (smFRET) is an important, increasingly utilized experimental technique [1–9] for studying protein disordered states, especially those of intrinsically disordered proteins (IDPs) [10–15]. Applications of smFRET to infer conformational dimensions of unfolded states of globular proteins [16–18] and IDPs [19–21] have provided insights into fundamental protein biophysics including, for example, folding stability and cooperativity [22–26], transition paths [27, 28], and compactness of IDP conformations [20, 21] involved in fuzzy complexes [29–32]. Single-molecule conformational dimensions likely bear as well on biologically functional liquid-liquid IDP phase separation [33] because the amino acid sequence-dependent single-chain compactness of charged IDPs [34, 35] are predicted by theory [36] to be closely correlated with these polyampholytic proteins’ tendency to undergo multiple-chain phase separation [37].

Basically, inference from smFRET data on measures of conformational dimensions such as radius of gyration R_g entails matching experimental average energy transfer efficiency $\langle E \rangle_{\text{exp}}$ with simulated (or analytically calculated) transfer efficiency $\langle E \rangle_{\text{sim}}$ predicted by a chosen polymer model. Using a Gaussian chain model or an augmented Sanchez mean-field theory, conventional smFRET inference procedures presume a homogeneous conformational ensemble that expands or contracts uniformly [17, 38, 39] in response to changes in solvent conditions such as denaturant concentration [40]. Such an interpretation of smFRET data stipulated a significant collapse of unfolded-state conformations, as quantified by a substantial decrease in R_g , upon changing solvent conditions from strongly unfolding to folding by lowering denaturant concentration [16, 17]. This smFRET prediction has led to a long-standing puzzle for Protein L [1, 41–43] because for this two-state folder [44], an apparently more direct measurement of R_g by small-angle X-ray scattering (SAXS) indicated that the average compactness of its unfolded-state conformational ensemble does not vary much with denaturant [1, 41]. Similar behaviors have also been observed in SAXS experiments on other proteins [45].

Although the smFRET-SAXS puzzle remains to be fully resolved, several advances since the discrepancy was first noted [16] have contributed to clarifying the pertinent issues. A study using explicit-chain models questioned the general validity of conventional “standard” smFRET interpretation by showcasing that it incurs substantial errors in inferred R_g [46]. A systematic analysis of subensembles of self-avoiding chains pinpointed the conventional procedure’s basic shortcoming in always presuming a homogeneous ensemble, an assumption that leads to grossly overestimated R_g ’s for small $\langle E \rangle_{\text{exp}}$ values [21]. Allowing for conformational heterogeneity, which is clearly observed in a number of smFRET experiments [18, 47], the subensemble analysis prescribes a “most probable” radius of gyration, R_g^0 , for any given $\langle E \rangle_{\text{exp}}$. When applied to an N-terminal IDP fragment of

the Cdk inhibitor Sic1 [29, 30, 32], the subensemble-inferred, denaturant-dependent R_g^0 is in good agreement with SAXS-determined R_g and NMR measurement of hydrodynamic radius, in contrast to conventional procedures that produced unphysical results [21].

Consistent with this conceptual framework that emphasizes conformational heterogeneity and polymer excluded volume, two other recent explicit-chain simulation studies also concluded that conventional smFRET inference of R_g is inadequate [48, 49]. Notably, the coarse-grained model simulation in ref. [48] predicted an ≈ 3.0 Å contraction of average R_g for Protein L upon diluting GuHCl from 7.5 M to 1.0 M. The authors surmised that 3.0 Å is “close to the statistical uncertainties” of SAXS-measured R_g values, and therefore a resolution of the smFRET-SAXS discrepancy for Protein L might be within reach [48]. More recently, an extensive experimental-computational study of a destabilized mutant of spectrin domain R17 and the IDP ACTR also underscored the importance of explicit-chain simulations in the interpretation of smFRET data. Denaturant-dependent expansion of conformational dimensions was consistently observed for these proteins from multiple experimental methods as well as in all-atom explicit-water molecular dynamics simulations [50, 51]. Protein L, however, was not the subject of this investigation.

In view of recent results that apparently affirm an appreciable denaturant-dependent R_g for unfolded proteins—albeit not as sharp as posited by conventional smFRET interpretation, is an essentially denaturant-independent average unfolded-state R_g as envisioned in the usual picture of cooperative protein folding tenable? To address this question, we determined computationally the distribution of R_g consistent with any given $\langle E \rangle_{\text{exp}}$ and the derived probabilities that different $\langle E \rangle_{\text{exp}}$ ’s are consistent with the same R_g ’s. Taking an agnostic view as to the merits of various experimental techniques, we invoked minimal theoretical assumption so as to let experimental data speak for themselves. Accordingly, our coarse-grained model incorporates only the most rudimentary geometry of polypeptide chains, without any detailed force field such as those applied in recent smFRET-related simulations [46, 48, 50]. By this very construction, our analysis is unaffected by any known or potential limitations of current coarse-grained and atomic force fields [14, 52–57]. As detailed below, we found that simple conformational statistics dictates a broad distribution of R_g for most $\langle E \rangle_{\text{exp}}$ ’s. Among such conditional distributions $P(R_g|\langle E \rangle_{\text{exp}})$ ’s for different $\langle E \rangle_{\text{exp}}$ values, large overlaps exist even for significantly different $\langle E \rangle_{\text{exp}}$ ’s. These results suggest that, even if published experimental data are taken at face value, conceivably the smFRET-SAXS discrepancy can be resolved provided sufficient denaturant-dependent conformational heterogeneity in the unfolded state is encoded by the amino acid sequence of the protein in question. Our analysis thus establishes a physical perimeter within which future experimental and theoretical smFRET analyses may proceed.

Methods

The C_α protein model and the sampling algorithm used here are the same as that in our previous study [21]. The protein is represented by a sequence of n beads connected by C_α - C_α virtual bonds of length 3.8 Å. The potential energy $E = \sum_{i=2}^{n-1} \epsilon_\theta(\theta_i - \theta_0)^2 + (1/2) \sum_{i=1}^n \sum_{j=1}^n \epsilon_{\text{ex}}(R_{\text{hc}}/R_{ij})^{12}$, where $\epsilon_\theta = 10.0k_{\text{B}}T$, θ_i is the virtual bond angle at bead i , $\theta_0 = 106.3^\circ$ is the reference that corresponds to the most populated virtual bond angle in the Protein Data Bank [58], k_{B} is the Boltzmann constant, T is the absolute temperature, $\epsilon_{\text{ex}} = 1.0k_{\text{B}}T$ is the model protein's self-avoiding excluded-volume repulsion strength, and $R_{ij} = |\mathbf{R}_j - \mathbf{R}_i|$ is the distance between beads i, j , wherein \mathbf{R}_i is the position vector for bead i . The excluded-volume $(R_{\text{hc}}/R_{ij})^{12}$ term is set to zero for $R_{ij} \geq 10.0$ Å. For the present study, we set the hard-core repulsion distance $R_{\text{hc}} = 4.0$ Å as in many protein folding simulations [24].

We conducted Monte Carlo sampling by applying the Metropolis criterion [59] at $T = 300$ K using an algorithm described previously [60] that assigns equal a priori probability for pivot and kink jumps [61, 62]. The acceptance rate for the attempted chain moves was $\approx 30\%$. The first 10^7 equilibrating attempted moves of each simulation were excluded from the tabulation of statistics. Subsequently, 10^9 moves were attempted for each chain length n we studied to sample 10^7 conformations for further analysis. Values of radius of gyration $R_g = \sqrt{n^{-1} \sum_{i=1}^n |\mathbf{R}_i - \mathbf{R}_{\text{cm}}|^2}$ (where $\mathbf{R}_{\text{cm}} = n^{-1} \sum_{i=1}^n \mathbf{R}_i$) and end-to-end distance $R_{\text{EE}} = |\mathbf{R}_n - \mathbf{R}_1|$ were computed for the sampled conformations to determine the distribution $P(R_g, R_{\text{EE}})$ of populations centered at various (R_g, R_{EE}) with only narrow ranges of variations (bins) around the given R_g and R_{EE} values.

We focus here only on cases in which the dyes are attached to the two ends of the protein chain. FRET efficiency for a given conformation in the model with end-to-end distance R_{EE} is then calculated by the formula

$$E(R_{\text{EE}}) = \frac{R_0^6}{R_0^6 + R_{\text{EE}}^6}, \quad (1)$$

where R_0 is the Förster radius of the dye. Based on the values of $R_0 = 54 \pm 3$ Å given by Sherman and Haran [16] and $R_0 = 54.0$ Å provided by Merchant et al. [17] for the Alexa 488 and Alexa 594 dyes employed in their Protein L experiments, we set $R_0 = 55$ Å in most of the computation for Protein L below. For any given distribution $P(R_{\text{EE}})$, the average FRET efficiency is given by $\langle E \rangle = \int dR_{\text{EE}} E(R_{\text{EE}})P(R_{\text{EE}})$. The subscripts in the above expressions $\langle E \rangle_{\text{exp}}$ and $\langle E \rangle_{\text{sim}}$ are omitted hereafter for notational simplicity when the meaning of the average $\langle E \rangle$ is clear from the textual context. Protein L is a 64-residue α/β protein. To account for the added effective chain length due to the two dye linkers, we used $n = 75$ chains to model the unfolded-state conformations of Protein

L. This prescription for the linkers is similar to the ten [63] or eight [17] extra residues used before. In addition to the exemplary computation for Protein L, simulations were also conducted for several other representative chain lengths ($n = 50, 100, 125$, and 150) and Förster radii ($R_0 = 50, 60$, and 70 Å) for future applications to other disordered protein conformational ensembles.

Results

Physicality of a subensemble approach to smFRET inference. To ensure that smFRET inference takes into account only physically realizable conformations, we recently introduced a systematic methodology to infer a most probable radius of gyration R_g^0 from an experimental $\langle E \rangle_{\text{exp}}$ by considering subensembles of self-avoiding walk (SAW) conformations with narrow ranges of R_g simulated using an explicit-chain model. For any such range (bin) centered around an R_g , the method provides a conditional distribution $P(R_{\text{EE}}|R_g)$ for the end-to-end distance R_{EE} . An average FRET efficiency $\langle E \rangle(R_g) = \int dR_{\text{EE}} E(R_{\text{EE}})P(R_{\text{EE}}|R_g)$ is then calculated. The most probable R_g^0 is determined by matching $\langle E \rangle_{\text{exp}}$ with $\langle E \rangle(R_g)$, viz., by solving the equation

$$\langle E \rangle(R_g^0) = \langle E \rangle_{\text{exp}} \quad (2)$$

for R_g^0 to arrive at $R_g^0(\langle E \rangle)$ (wherein the “exp” is dropped from the average), which is the inverse function of $\langle E \rangle(R_g)$. As documented before [18, 21] and outlined above, by explicitly allowing for unfolded-state conformational heterogeneity—which is expected physically [14, 15], the subensemble SAW method circumvents the limitations of conventional smFRET inferences that presuppose a homogeneous conformational ensemble [16, 17, 39].

Based on the same conceptual framework, here we approach the question of smFRET inference from a complementary angle. Instead of starting from subensembles with a narrow range of R_g to derive $P(R_{\text{EE}}|R_g)$, then $\langle E \rangle(R_g^0)$ and then $R_g^0(\langle E \rangle)$, here we start from subensembles with a narrow range of R_{EE} (smallest bin size = 0.5 Å, see below), and hence a narrow variation of E (i.e., via Eq. (1), the E values in a narrow range may be taken as a single E value), to derive distribution $P(R_g|R_{\text{EE}})$ conditioned upon R_{EE} . While $P(R_g|R_{\text{EE}})$ is related to $P(R_{\text{EE}}|R_g)$ by Bayes’ theorem, $P(R_g|R_{\text{EE}})$ is of interest because it quantifies directly the possible variation in conformational dimensions when only a single $\langle E \rangle_{\text{exp}}$ value is known. This is because for every single FRET efficiency E , the quantity $P(R_g|R_{\text{EE}})$ is sufficient to provide the conditional distribution $P(R_g|E)$. Then, based on these derived $P(R_g|E)$ distributions for all individual E values, the $P(R_g|\langle E \rangle_{\text{exp}})$ distribution conditioned upon any value of $\langle E \rangle_{\text{exp}}$ averaged from any underlying distribution $P(E)$ of E can be readily obtained.

Estimation of conformational dimensions from FRET efficiency is highly model dependent because of insufficient structural constraint. As an exemplary case, we applied this formulation to Protein L. Figure 1 shows that different inference approaches lead to very different pictures of how the average radius of gyration, $\langle R_g \rangle$, of this protein varies with denaturant concentration. For a change in [GuHCl] from ≈ 7 M to ≈ 2 M, conventional inference (diamonds) yielded large $\langle R_g \rangle$ decreases of ≈ 9 Å (filled diamonds, ref. [16]) or ≈ 5 Å (open diamonds, ref. [17]). In contrast, subensemble SAW methods (circles) stipulate a much milder variation with respect to [GuHCl]. For the same [GuHCl] change, the most probable R_g^0 value decreases by ≈ 2 Å (open circles) whereas the change in root-mean-square $\sqrt{\langle R_g^2 \rangle} \equiv \{\int dR_g R_g^2 P(R_g | \langle E \rangle_{\text{exp}})\}^{1/2}$ conditioned upon the published experimental $\langle E \rangle_{\text{exp}}$ data is even smaller: it decreases by ≈ 1 Å (filled circles). When [GuHCl] is reduced further from 2 M to 0 M, the total decrease over the entire [GuHCl] range is ≈ 5.5 Å for R_g^0 but merely ≈ 2 Å for $\sqrt{\langle R_g^2 \rangle}$. We computed distributions of R_g^2 and $\sqrt{\langle R_g^2 \rangle}$ here because these quantities are determined by SAXS [45, 64]. Our results are essentially unchanged if $\langle R_g \rangle$ is considered instead (see below).

For every $\langle E \rangle_{\text{exp}}$ data point we considered for Protein L using subensemble analysis, significant diversity in R_g^2 values that are nonetheless consistent with the given $\langle E \rangle_{\text{exp}}$ is observed (Fig. 1, error bars for filled circles). These large variations in inferred R_g^2 values and the large overlaps of the ranges of these variations at different [GuHCl]’s imply that significant fractions of the unfolded conformational ensembles of Protein L at different [GuHCl]’s can encompass conformations with very similar R_g ’s. Notably, the average R_g expected of a fully unfolded protein in good solvent of the same length as Protein L with dye linkers (horizontal dashed line, ref. [65]) is within the $\sqrt{\langle R_g^2 \rangle}$ error bars for [GuHCl] as low as 3 M. Even at zero denaturant, the $R_g \approx 24.5$ Å value (upper error bar), at one standard deviation from the mean, $\sqrt{\langle R_g^2 \rangle}$, is only ≈ 1 Å from the average R_g expected of a fully unfolded conformational ensemble.

Conformations consistent with a given FRET efficiency generally have highly diverse radii of gyration. The diversity in R_g values that are consistent with a given R_{EE} (and therefore a given $\langle E \rangle$) is further illustrated in Fig. 2. For our Protein L model, the square root of the standard deviation in R_g^2 , $\sqrt{\sigma(R_g^2)}$, is substantial for the entire range of R_{EE} : It increases steadily from ≈ 8 Å for $R_{\text{EE}} \approx 0$ to ≈ 12 Å for $R_{\text{EE}} \approx 120$ Å (Fig. 2b). Therefore, although $\sqrt{\langle R_g^2 \rangle}$ of the conformations consistent with a given R_{EE} increases monotonically from ≈ 18 to ≈ 37 Å over the R_{EE} range in Fig. 2a, knowledge of R_{EE} alone can barely narrow down the wide range of possible R_g values and vice versa (Fig. 2c–f).

A panoramic view of the logic of smFRET inference on conformational dimensions

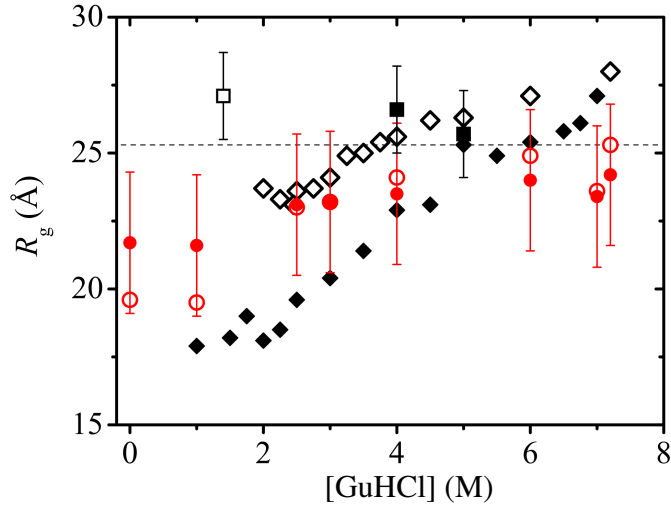


FIG. 1: Unfolded-state dimensions of Protein L obtained from SAXS and various interpretations of smFRET experiments. Open and filled squares are results from previous time-resolved and equilibrium SAXS experiments by Plaxco et al. at $2.7 \pm 0.5^\circ\text{C}$ and $5 \pm 1^\circ\text{C}$, respectively. The associated error bars represent one-standard-deviation fitting uncertainties (kinetic data) or confidence intervals from two to three independent measurements (thermodynamic data) [44]. Subsequent equilibrium SAXS measurement at 22°C by Yoo et al. [41] produced essentially identical results. Open and filled diamonds are results from smFRET experiments, respectively, by Merchant et al. (Eaton group, temperature not provided) [17] and by Sherman and Haran conducted at “room temperature” [16]. These prior experimental data were compared in a similar manner in ref. [41]. Here, the open and filled circles are from our analysis corresponding, respectively, to the most-probable R_g^0 (ref. [21]) and the root-mean-square $\sqrt{\langle R_g^2 \rangle}$ based on the experimental transfer efficiency $\langle E \rangle = 0.74$ for $[\text{GuHCl}] = 0$ given by Merchant et al., the $\langle E \rangle$ values for Protein L (corrected from the measured FRET efficiency $\langle E_m \rangle$) in Table 2 of Supporting Information for the same reference [17], and the $\langle E \rangle$ values for $[\text{GuHCl}] = 1 \text{ M}$ and 7 M in Sherman and Haran [16]. A Förster radius of $R_0 = 55 \text{ \AA}$ was used in our calculations. The error bars for the open squares span ranges delimited by $\sqrt{\langle R_g^2 \rangle} \pm \sigma(R_g^2)$ where $\sigma(R_g^2)$ is the standard deviation of the distribution of R_g^2 at the given E value. The horizontal dashed line marks the $R_g = 25.3 \text{ \AA}$ value we obtained from applying the scaling relation of Kohn et al. [65] to $N = 74$, where $n = N + 1 = 75$ is taken to be the equivalent number of amino acid residues for Protein L plus dye linkers.

is provided by Fig. 3, wherein $P(R_g, R_{\text{EE}})$ is converted to $P(R_g, E)$ by Eq. (1). Using our model for unfolded Protein L as an example, the landscape in the top panel of Fig. 3 shows clearly that the R_g – E scatter is wide, with the most populated (red) region elongated mainly along the E axis with a small negative incline. Consistent with Fig. 1, this population distribution implies that even large variations in E do not necessitate much change in the R_g distribution. This feature of the R_g – E space is demonstrated

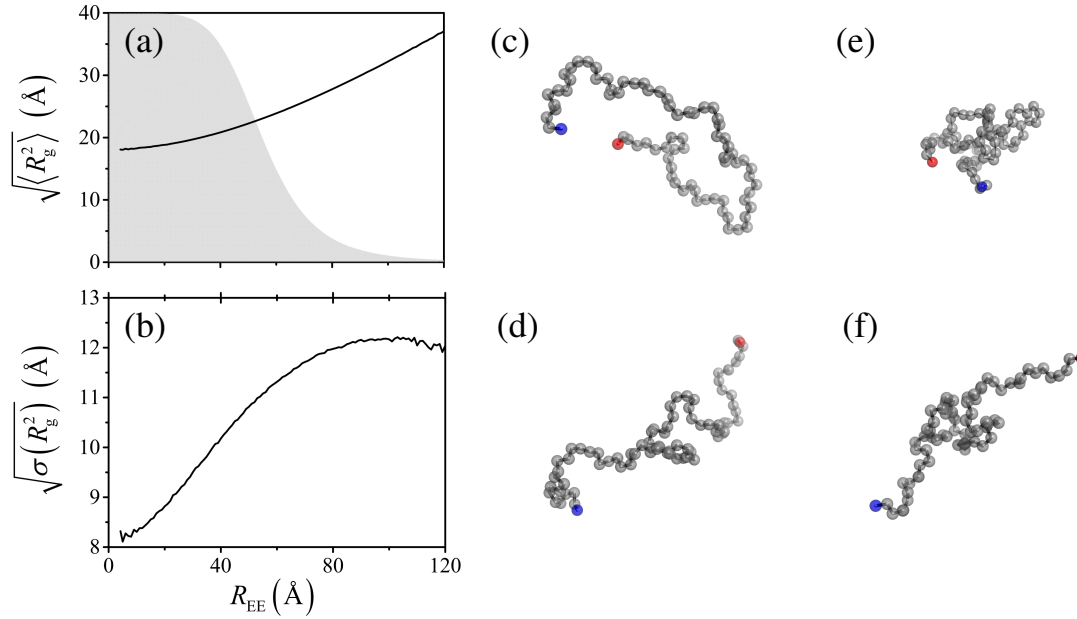


FIG. 2: Large variations in dimensions among conformations with a given end-to-end distance R_{EE} . (a) Root-mean-square $\sqrt{\langle R_g^2 \rangle}$ and (b) the square root of the standard deviation of R_g^2 as functions of R_{EE} . The grey profile in (a) shows the theoretical transfer efficiency Eq. (1) for $n = 75$ and $R_0 = 55$ Å in a vertical scale ranging from zero to unity. (c)–(f) Example conformations with the red and blue beads marking the termini of $n = 75$ chains. They serve to illustrate the possible concomitant occurrences of (c) small $R_{EE} = 19.7$ Å and large $R_g = 26.3$ Å; (d) large $R_{EE} = 80.1$ Å and large $R_g = 26.2$ Å; (e) small $R_{EE} = 19.7$ Å and small $R_g = 14.2$ Å; as well as (f) large $R_{EE} = 80.4$ Å and small $R_g = 19.8$ Å.

more specifically by the $\sqrt{\langle R_g^2 \rangle(E)}$ curve in the bottom panel of Fig. 3 (red solid curve; the dependence of $\langle R_g \rangle$ on E is essentially identical, blue solid curve), wherein an overwhelming majority of E values are seen to be consistent with R_g values between 20 and 27 Å that are within one standard deviation of $\sqrt{\langle R_g^2 \rangle(E)}$ (red dashed curves). It is noteworthy that, for most E values, the variation of $\sqrt{\langle R_g^2 \rangle(E)}$ is milder than that of $R_g^0(\langle E \rangle)$; i.e., $|d\sqrt{\langle R_g^2 \rangle}/dE| < |dR_g^0/d\langle E \rangle|$. In fact, this trend is already evident in Fig. 1 from the milder [GuHCl] dependence of $\sqrt{\langle R_g^2 \rangle}$ (filled circles) than that of R_g^0 (open circles).

Conformations sharing similar radii of gyration can have very different FRET efficiencies. In light of the large diversity in R_g values conditioned upon a given E and the very mild variation of $\sqrt{\langle R_g^2 \rangle}$ and $\sigma(R_g^2)$ with E (Fig. 3), one expects that conformations consistent with even very different E values share highly overlapping R_g

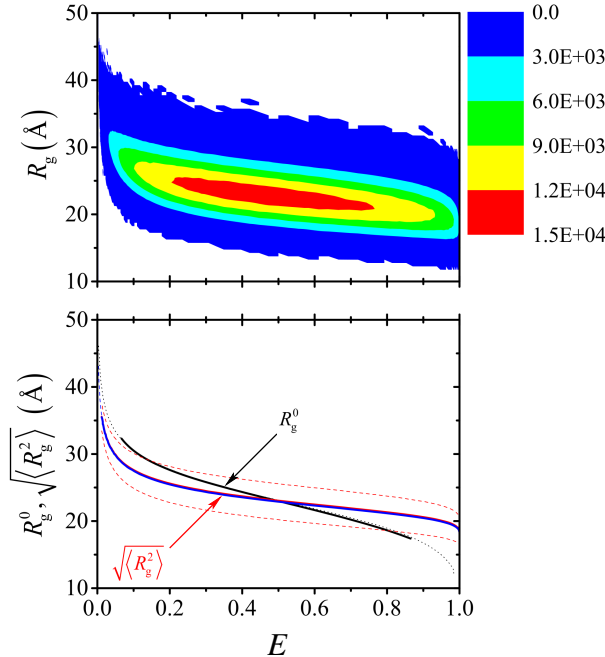


FIG. 3: Perimeters of inference on conformational dimensions from Förster transfer efficiency. Top: Distribution $P(R_g, E)$ of conformational population as a function of R_g and E for $n = 75$ and $R_0 = 55$ Å. The distribution was computed using $R_{EE} \times R_g$ bins of $1.0\text{\AA} \times 0.5\text{\AA}$. White area indicate bins with no sampled population. Bottom: Most-probable radius of gyration $R_g^0(\langle E \rangle)$ from our previous subensemble SAW analysis [21] (black solid curve) compared against root-mean-square radius of gyration $\sqrt{\langle R_g^2 \rangle}(E)$ (red solid curve) computed by considering 30 subensembles with narrow ranges of R_{EE} . The latter overlaps almost completely with $\langle R_g \rangle(E)$ computed using the same set of subensembles (blue solid curve). The $R_g(\langle E \rangle)$ (black dotted curve) and $\langle R_g \rangle(E)$ (blue dashed curve) were obtained from the top distribution, respectively, by averaging over E at given R_g values and by averaging over R_g at given E values. Variation of radius of gyration is illustrated by the red dashed curves for $\sqrt{\langle R_g^2 \rangle} \pm \sigma(R_g^2)$ as functions of E . The essential coincidence between the black solid and dotted curves and between the blue solid and dotted curves indicate that the present results are robust with respect to the choices of bin size we have made. Note that the black solid curve for $R_g^0(\langle E \rangle)$ does not cover $\langle E \rangle$ values close to zero or close to unity because larger R_g bin sizes ($\sim 1.1\text{--}3.6$ Å) than the current R_g bin size of 0.5 Å were used (Table S5 of ref. [21]), thus precluding extreme values of $\langle E \rangle$ to be considered in that previous $n = 75$ subensemble SAW analysis [21]. This limitation is now rectified for $n = 75$ (black dotted curve).

values. We now characterize this overlap quantitatively by first considering two sharply defined representative R_{EE} values in Fig. 4a (vertical bars depicting δ -function-like distributions) that correspond, by virtue of Eq. (1), to two sharply defined E values ≈ 0.45 and 0.75 (Fig. 4b). These E values are representative because they coincide with the experimental $\langle E \rangle_{\text{exp}}$ for Protein L at $[\text{GuHCl}] = 7$ M and 1 M, respectively [16]. The con-

ditional distributions $P(R_g^2|E)$ for $E = 0.45$ and $E = 0.75$ overlap significantly, with the overlapping area ≈ 0.75 (Fig. 4c). By definition, this area is the overlapping coefficient, OVL, used in statistical analysis for measuring similarity between distribution [66]. OVL between two distributions is generally given by

$$\text{OVL}_{1,2} = \int dx \min[P_1(x), P_2(x)] , \quad (3)$$

where $P_1(x)$ and $P_2(x)$ are two normalized distributions of variable x . The P_1 , P_2 distributions are $P(R_g^2|E = 0.45)$ and $P(R_g^2|E = 0.75)$ in Fig. 4c.

Because experimentally determined E values are often averages, not sharply defined [16, 17], it is necessary to address more realistic distributions of E on smFRET inference. We do so here by considering hypothetical broad Gaussian distributions for R_{EE} centered around the two sharply defined R_{EE} values (Fig. 4a, curves, standard deviation $\sigma(R_{\text{EE}}) = 20.3 \text{ \AA}$), resulting in broad distributions in E averaging to $\langle E \rangle = 0.45$ and 0.74 (Fig. 4b, curves), which are essentially equal to the sharply defined E values of 0.45 and 0.75. Modifying the two sharply defined E values to two broad distributions of E has very little impact on either the individual distributions of R_g^2 or the overlap of the two $P(R_g^2)$ distributions (Fig. 4d). The overlapping coefficient remains ≈ 0.75 .

Although the distributions in Fig. 4c and 4d are very similar, there is a basic difference between two sharply defined E values and two broad distributions of E in regard to the conformations in the R_g^2 distributions. When the E values are sharply defined, there is no overlap in the actual conformations in the two $P(R_g^2|E)$ distributions because the conformational ensembles consistent with two sharply defined R_{EE} values are disjoint. However, when the two sets of E values are broadly distributed with overlapping R_{EE} and E values (Fig. 4a, b; curves), some of the conformations from the two different R_g^2 distributions that contribute to the overlapping region in Fig. 4d can be identical.

The distribution of radius of gyration consistent with a given single FRET efficiency is very similar to that consistent with a symmetric distribution of FRET efficiencies centered around it. This insensitivity of the distribution of R_g^2 (and therefore also of R_g) conditioned upon given E values to variations in the width of Gaussian-like distribution of E is not difficult to fathom. Given the mild variation of $\sqrt{\langle R_g^2 \rangle}$ and $\sigma(R_g^2)$ with respect to E (Fig. 3, bottom panel) and the tendency for effects from E values on opposite sides of the average of a symmetric distribution to cancel each other, averaging over a range of E values centered around a given E ($= \langle E \rangle$) is not expected to result in an overall average R_g^2 and overall distribution width that are substantially different from those for a sharply defined $E = \langle E \rangle$. For the sake of testing the robustness of this insensitivity, here we have used a large standard deviation,

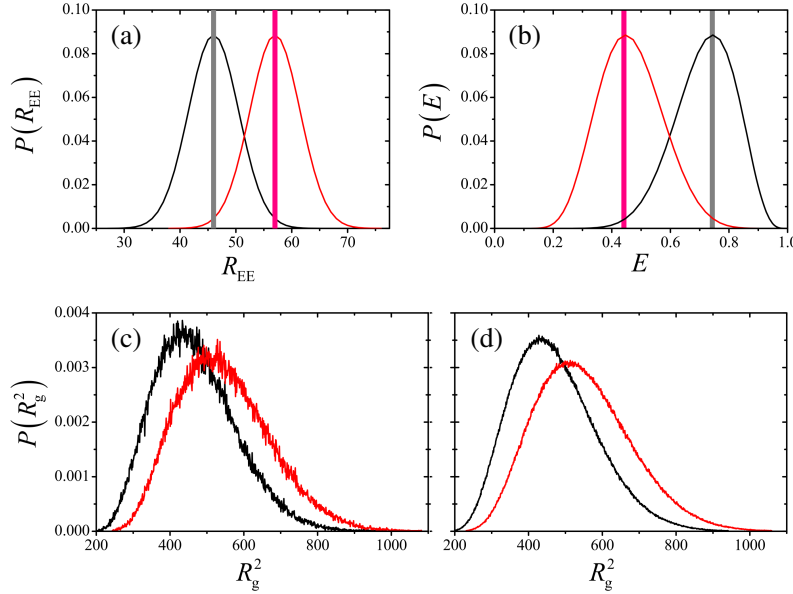


FIG. 4: Substantially overlapping distributions of conformational dimensions can be consistent with very different Förster transfer efficiencies. (a) Hypothetical distributions $P(R_{\text{EE}})$ of end-to-end distance R_{EE} . Two hypothetical sharp distributions at two R_{EE} values (vertical bars) and two hypothetical broad Gaussian distributions (bell curves) centered at these two R_{EE} values, with standard deviation of the Gaussian distributions chosen to be 20.3 \AA . (b) The corresponding distribution $P(E)$ of Förster transfer efficiency E . The left and right sharp distributions of $P(R_{\text{EE}})$ in (a) lead, respectively, to $E \approx 0.745$ (right) and $E \approx 0.447$ (left) in (b). The corresponding $P(E)$ for the hypothetical Gaussian distributions in (a) entail broad distributions in (b) with mean values at $\langle E \rangle = 0.735$ (right) and $\langle E \rangle = 0.453$ (left) respectively. (c) The left and right curves are the conditional distributions $P(R_g^2|E)$, respectively, for the sharply defined $E \approx 0.745$ and $E \approx 0.447$ in (b). (d) Similar to (c) except the distributions of R_g^2 are now for the two broad $P(E)$ distributions in (b). The R_g^2 bin size in (c) and (d) is 1.0 \AA^2 . The overlap area (OVL) of the two normalized distribution curves in (c) and (d) are, respectively, 0.747 and 0.754. The percentages of population with $R_g^2 \geq 625 \text{ \AA}^2$ in the distributions in (c) and (d) are, respectively, 9.2% and 10.1% for $E \approx 0.745$ and $\langle E \rangle = 0.735$, and 25.2% and 26.3% for $E \approx 0.447$ and $\langle E \rangle = 0.453$.

$\sigma(R_{\text{EE}})$, for the hypothetical Gaussian distributions in Fig. 4a. This $\sigma(R_{\text{EE}})$ is equal to the standard deviation of the R_{EE} distribution for the full conformational ensemble (with the mean, $\langle R_{\text{EE}} \rangle = 59.1 \text{ \AA}$). Beside the R_{EE} and E distributions in Fig. 4, we performed additional calculations using Gaussian distributions of R_{EE} centered at different averages, with different standard deviations that equal $0.1 \times$, $0.25 \times$, $0.5 \times$, and $0.75 \times \sigma(R_{\text{EE}})$. These constructs beget distributions of E with different $\langle E \rangle$ values. In all cases we considered, the resulting R_g^2 distribution for the given $\langle E \rangle$ is essential the same across the different standard deviations as well as for the case with a sharply defined $E = \langle E \rangle$.

This finding suggests that the $\sqrt{\langle R_g^2 \rangle(E)} - E$ dependence in Fig. 3 (bottom panel) is not strictly limited to sharply defined E values. An essentially identical relationship should also be applicable to the $\sqrt{\langle R_g^2 \rangle(\langle E \rangle)}$ and associated $\sigma(R_g^2)$ conditioned upon reasonably symmetric distributions of E with mean value $\langle E \rangle$. In other words, $\sqrt{\langle R_g^2 \rangle(E)}$ in Fig. 3, which was originally constructed for sharply defined E values, is also expected to be a good approximation of $\sqrt{\langle R_g^2 \rangle(\langle E \rangle)}$ for essentially symmetric distributions of E . More generally, the $\sqrt{\langle R_g^2 \rangle(\langle E \rangle)}$ for any distribution $P(E)$ of E , symmetric or otherwise, can be calculated readily as $[\int dE P(E) \langle R_g^2 \rangle(E)]^{1/2}$ by using the $\langle R_g^2 \rangle(E)$ values from Fig. 3.

Inference of conformational dimensions solely from FRET efficiency can entail significant ambiguity. To ascertain more generally the degree to which the R_g values consistent with different FRET efficiencies overlap, we extended the comparison in Fig. 4c for two E values by computing the corresponding overlapping coefficients (Eq. (3)) for all possible pairs of FRET efficiencies, E_1 and E_2 :

$$\text{OVL}(R_g^2)_{E_1, E_2} = \int dR_g^2 \min[P(R_g^2|E_1), P(R_g^2|E_2)]. \quad (4)$$

The heat map in Fig. 5 indicates substantial overlaps for a majority of (E_1, E_2) . Among all possible (E_1, E_2) combinations, more than 30% have $\text{OVL} \geq 0.8$, and close to 60% have $\text{OVL} \geq 0.6$ (Fig. S1a), meaning that their $P(R_g^2|E)$'s are quite similar. We also computed averages of R_g^2 over the overlapping regime of the pairs of distributions. These averages represent conformational dimensions that are consistent with both E_1 and E_2 . In a majority of the situations, the root-mean-square R_g^2 for the overlapping regime stays within a relative narrow range of $\approx 22\text{--}25 \text{ \AA}$ for our model of unfolded Protein L, even for E_1 and E_2 that are quite far apart (Fig. S1b). Therefore, taken together with Figs. 1–4, the overview in Fig. 5 indicates that when an explicit-chain physical model is used to interpret/rationalize smFRET data [18, 21], as is the case here, the a priori expectation is that even substantial changes in $\langle E \rangle_{\text{exp}}$ do not necessarily imply large changes in average R_g . In this light, previous smFRET-based stipulations of large denaturant-dependent changes in the $\langle R_g^2 \rangle$ of Protein L [16, 17] is demonstratively inconclusive in the absence of additional relevant experimental information, because they were based on conventional inference approaches that are not entirely physical [21]. Moreover, as is evident from the examples in Fig. 6, the trend of a mild $R_g - E$ variation that we saw previously [21] and in Figs. 1–5 here, which is derived directly from explicit-chain polymer models, is expected to hold generally for other FRET systems of disordered proteins with different chain lengths and Förster radii as well.

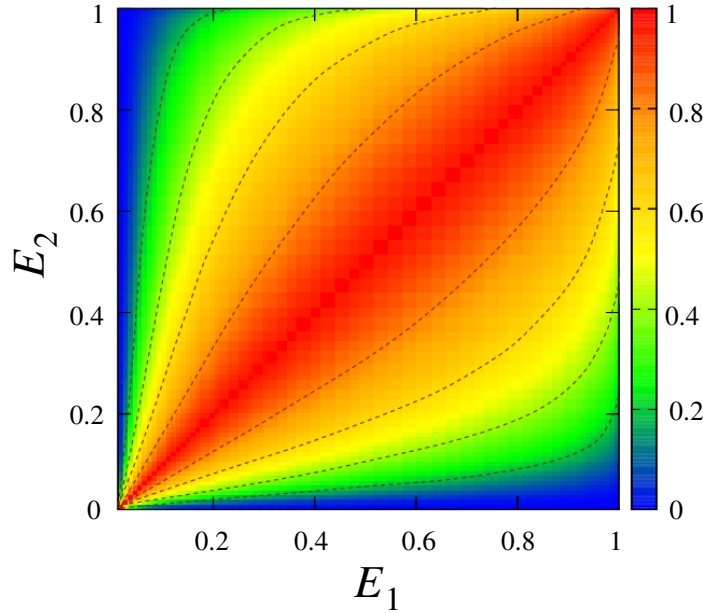


FIG. 5: Ambiguities in FRET inference of conformational dimensions. The heat map provides for $n = 75$ and $R_0 = 55$ Å the overlapping coefficient $\text{OVL}(R_g^2)_{E_1, E_2}$ of pairs of R_g^2 distributions conditioned upon FRET efficiencies E_1 and E_2 . Contours on the heat map are for $\text{OVL}(R_g^2)_{E_1, E_2} = 0.8, 0.6, 0.4$, and 0.2 , as indicated by the color scale on the right.

Discussion

Subensemble-derived conditional distributions of R_g are basic to smFRET inference. To recapitulate, here we have further developed the subensemble SAW approach to smFRET inference of conformational dimensions [21], which is based on the obvious principle that only physically realizable conformational ensembles should be invoked to interpret smFRET data. We focused previously on the most probable radius of gyration $R_g^0(\langle E \rangle)$, which is derived from distributions of E conditioned upon a narrow range of R_g . Here we have considered the complementary quantity, $\sqrt{\langle R_g^2 \rangle(E)}$, which is the root-mean-square value of R_g conditioned upon a given E . These quantities are not identical, but their variations with $\langle E \rangle$ or E are similar (Figs. 3 and 6). Relative to conventional approaches to smFRET inference, both $R_g^0(\langle E \rangle)$ and $\sqrt{\langle R_g^2 \rangle(E)}$ exhibit a milder dependence on smFRET efficiency, covering a range of R_g values consistent with polymer physics [21]. By construction, $R_g^0(\langle E \rangle)$ is appropriate if it is known or it is presumed that the disordered conformations populate a narrow range of R_g values or distribute symmetrically around an average R_g [21], whereas $\sqrt{\langle R_g^2 \rangle(E)}$ is suitable when

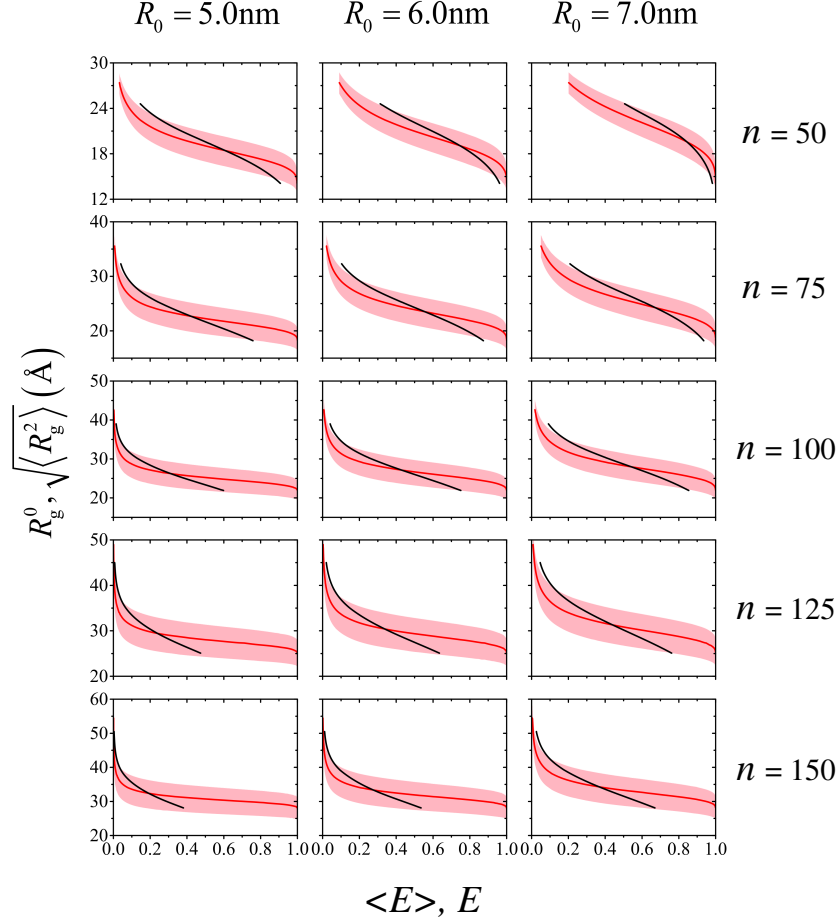


FIG. 6: Most probable and root-mean-square radius of gyration. Generalization of the $R_g^0(\langle E \rangle)$ (solid black curves), and $\sqrt{\langle R_g^2 \rangle(E)}$ (solid red curves) for $R_0 = 55 \text{ \AA}$ and $n = 75$ in Fig. 3 to other Förster radii R_0 and chain lengths n . The shaded areas are bound by $\sqrt{\langle R_g^2 \rangle(E)} \pm \sigma(R_g^2(E))$, which were represented by red dashed curves in Fig. 3. As discussed in the text, the $\sqrt{\langle R_g^2 \rangle(E)}$ curves computed here for sharply defined E values are expected to apply also to $\sqrt{\langle R_g^2 \rangle(\langle E \rangle)}$ for essentially symmetric distributions of E where $\langle E \rangle$ denotes the mean value of E in such distributions. As pointed out above for Fig. 3, the black $R_g^0(\langle E \rangle)$ curves shown here do not cover $\langle E \rangle$ values close to zero or unity because of the relatively large R_g bin sizes used previously [21].

such knowledge or assumption is absent. It is our contention that, given a single $\langle E \rangle_{\text{exp}}$ and in the absence of additional experimental data, the a priori quantities $R_g^0(\langle E \rangle)$ or $\sqrt{\langle R_g^2 \rangle(E)}$ should serve well as physically valid inferences. The data provided in Fig. 6 and the Supporting Information of ref. [21], as well as those in the present Figs. 3 and 6 are useful for this purpose.

Physically valid interpretation of smFRET data requires explicit-chain modeling. Conventional approaches to smFRET inference neglects possible sequence-dependent conformational heterogeneity of unfolded ensembles. They always enforce a full conformational ensemble that expands or contracts homogeneously [16, 17]. Lacking an explicit-chain representation, this elementary unphysicality of conventional smFRET inference was often overlooked. Consequently, when $\langle E \rangle_{\text{exp}}$ is small, these procedures force the entire ensemble to expand, leading to unrealistically high inferred $\langle R_g \rangle$ values [21]. Although conformations with large R_{EE} (and hence small E or $\langle E \rangle$) and large R_g are part of our subensemble analysis (e.g. Fig. 2f), these rare conformations in our simulations did not arise from physically unrealistic long Kuhn lengths or unrealistic intrachain repulsion as in conventional approaches [21]. This is the fundamental reason why conventionally inferred $\langle R_g \rangle$ values differ from those simulated using physical, explicit-chain models [18, 21, 46, 48, 49], and that such simulations, for Sic1 [21] and Protein L [48] for example, produced smaller variations in $\langle R_g \rangle$ consistent with the limits prescribed by our subensemble SAW analysis [21].

In this perspective, recent computational investigations using explicit-chain simulations to rationalize smFRET data represent significant advances. These efforts include a study on Protein L using a denaturant-dependent construct based on a native-centric G_0 -like sidechain potential [48] and an all-atom, explicit-water molecular dynamics study on ACTR and an R17 variant [50, 51]. In these studies, the conformational heterogeneity of unfolded/disordered ensembles encoded by amino acid sequences is taken into account either by a structure-specific G_0 -like potential [48] or a transferrable atomic force field [50, 51]. However, it should be emphasized that commonly used force fields may not capture the high degrees of folding cooperativity observed for real proteins [24]. In particular, in comparison with experiment, the disordered conformational ensembles predicted by several atomic force fields are too compact [25, 52, 54, 67]. Efforts to address this shortcoming is underway [55–57]. For the case of Protein L, an earlier study [53] using a denaturant-dependent coarse-grained sidechain model similar to the one used in the recent study by Maity and Reddy [48] suggests that, even with an essentially native-centric potential, the model is insufficiently cooperative vis-à-vis experiment. Specifically, the predicted chevron plot for Protein L has a folding-arm rollover [53], which is absent in experiment [44]. This behavior is related to denaturant-dependent shifts in the positions of transition and unfolded states in the model [53], which would likely lead to a reduction in $\langle R_g \rangle$ with decreasing [GuHCl]. We view these known limitations of current potentials for protein folding simulation as part of the very puzzle underscored by the smFRET-SAXS discrepancy. The crux of the matter is, if the degrees of folding cooperativity for some—albeit not all—proteins, such as Protein L, are indeed as high as envisioned by SAXS measurements [44], why can't common force fields capture the phenomenon [53]?

In lieu of attempting to provide an accurate model of sequence-specific interactions, our subensemble SAW approach to smFRET inference does not presume any particular model of sequence-dependent conformational heterogeneity. By itself, our approach merely establishes a perimeter for physically realizable conformational variation [21]. The rationale is to let experiment take precedence in uncovering the actual conformational heterogeneity. In other words, $P(R_g^2|E)$ is a baseline distribution upon which any re-weighting of conformational population by sequence-specific effects is to be considered without pre-judgement. Under this conceptual framework, we make no generalization as to whether conformational dimensions of disordered proteins would or would not increase with increasing denaturant concentration. Such a verdict has to be made on a case-by-case basis depending on the nature of available experimental information in addition to the limited structural constraint provided by smFRET. For example, our previous study indicates that the dimensions of IDP Sic1 increases when [GuHCl] is increased from 1 M to 5 M [21]. A more recent in-depth study using smFRET, SAXS as well as other experimental probes and computation has demonstrated convincingly that conformational dimensions of the IDP ACTR and a destabilized mutant of globular protein R17 increase upon increasing [GuHCl] or [urea] [50, 51]. It is of relevance, however, that unlike Protein L [44], R17 is not a two-state folder as its chevron plot has a nonlinear unfolding arm [68].

A hypothetical scenario for the case of Protein L. To make conceptual progress in understanding the Protein L unfolded state, we now first put aside potential experimental artifacts that might be caused, for example, by the sensitivity of R_g to the fitting range of the Guinier analysis and the difficulty in obtaining low-denaturant SAXS data [51]. We assume, for the following consideration, that the SAXS-based finding of an essentially denaturant-independent $\langle R_g \rangle \approx 25 \text{ \AA}$ (ref. [44]) and the smFRET data of a decreasing $\langle E \rangle_{\text{exp}}$ with increasing denaturant [16, 17] are both valid. Under this premise, what we should seek is to rationalize the experimental data by denaturant-dependent heterogeneous conformational ensembles consistent with both sets of data, following an investigative logic commonly practised in the construction of putative unfolded and IDP ensembles [51, 69–71]. A solution to the smFRET-SAXS puzzle may then be possible if, with decreasing denaturant, sequence-specific effects become increasing biased to redistribute conformational population to high R_g^2 values to maintain a nearly constant $\langle R_g^2 \rangle$ despite the shift of the a priori, baseline $P(R_g^2|\langle E \rangle)$ distribution (prior to any re-weighting by sequence effect) to lower R_g^2 values due to the increase in $\langle E \rangle_{\text{exp}}$ with decreasing denaturant, a shift highlighted by Fig. 4.

How strong does such a denaturant-dependent conformational bias need to be? Using the example in Fig. 4, which is based on smFRET efficiencies of unfolded Protein L at $[\text{GuHCl}] = 1 \text{ M}$ and 7 M , an accounting of the bias needed to resolve the smFRET-

SAXS puzzle may be estimated. The a priori baseline $P(R_g^2|E)$ (Fig. 4c) and $P(R_g^2|\langle E \rangle)$ (Fig. 4d) distributions before imposition of any sequence-specific effect show that $\approx 10\%$ and $\approx 25\%$, respectively, of the $E, \langle E \rangle_{\text{exp}} \approx 0.74$ and $E, \langle E \rangle_{\text{exp}} \approx 0.45$ populations have $R_g^2 \geq 625 \text{ \AA}^2$, i.e., have $R_g \geq 25 \text{ \AA}$. It follows that if the actual, sequence-specific re-weighted distribution is to be consistent with the SAXS finding, possible shapes (among many) of the re-weighted, more restricted distributions may, for example, take the form of the shaded symmetric distributions in Fig. 7 because both of these distributions (pink plus grey, and grey shaded regions), centered at $R_g^2 = 625 \text{ \AA}^2$, have root-mean-square radius of gyration = 25 Å. The conformations in these restricted distributions can be selected such that the average $\langle E \rangle$ values over the restricted distributions are essentially identical to the original baseline distributions, i.e., $\langle E \rangle \approx 0.45$ for the pink plus grey distribution and $\langle E \rangle \approx 0.74$ for the grey distribution, by using the following construction.

We first consider restricted symmetric distributions, denoted as $P_r(R_g^2|E)$, that are of similar shapes, centered at $R_g^2 = 625 \text{ \AA}^2$, and are imposed upon $P(R_g^2|E)$ for sharply defined E values (such as those shown in Fig. 4c). Specifically, $P_r(R_g^2|E) = P(R_g^2|E)$ for $R_g^2 \geq 625 \text{ \AA}^2$ and $P_r(R_g^2|E) = \min[P(R_g^2|E), P(\{2 \times 625 \text{ \AA}^2 - R_g^2\}|E)]$ for $R_g^2 < 625 \text{ \AA}^2$. Note that $P_r(R_g^2|E)$ is not normalized. Performing the integral $\int dE P(E)P_r(R_g^2|E)$ for the two $P(E)$ distributions in Fig. 4b would then produce approximately the two restricted distributions in Fig. 7: By definition the integral gives exactly the $R_g^2 \geq 625 \text{ \AA}^2$ parts (darker shade) of the restricted distributions in Fig. 7, because in those regions the restricted distributions are identical to the corresponding $P(R_g^2|\langle E \rangle)$ distributions. The integral yields close approximations to the $R_g^2 < 625 \text{ \AA}^2$ parts (lighter shade) of the restricted distributions in Fig. 7 because of the mild and smooth variation of $\sqrt{\langle R_g^2 \rangle(E)}$ with E in the range $0.2 \leq E \leq 0.95$ (Fig. 3, lower panel) that covers most of the two $P(E)$ distributions in Fig. 4b. Constructed in this manner, the two conformational populations in the two restricted ensembles indicated by the shaded distributions in Fig. 7 preserve the two $\langle E \rangle = \int dE EP(E)$ values because the integral $\int dE P(E)P_r(R_g^2|E)$ preserves the average E at every R_g^2 . In other words, the shaded distributions in Fig. 7 (grey plus pink and grey) are now constructed to have different $\langle E \rangle \approx 0.45$ and $\langle E \rangle \approx 0.74$ but possess the same 25 Å as root-mean-square R_g nonetheless. Two examples of conformations in these restricted ensembles are provided in Fig. 7. Taken together, this hypothetical scenario suggests that consistency between SAXS and smFRET findings is perceivable if sequence-induced heterogeneity entails a mild restriction to $\sim 2 \times 25\% = 50\%$ of a priori conformational possibilities at $[\text{GuHCl}] = 7 \text{ M}$ but imposes a more severe restriction to $\sim 2 \times 10\% = 20\%$ of a priori conformational possibilities at $[\text{GuHCl}] = 1 \text{ M}$ (Fig. 7).

The biases represented by these numbers, which do not seem excessive, are intuitively plausible. Because they are derived using our coarse-grained C_α formulation, these fractional conformational restrictions should only be viewed as rough estimates. The

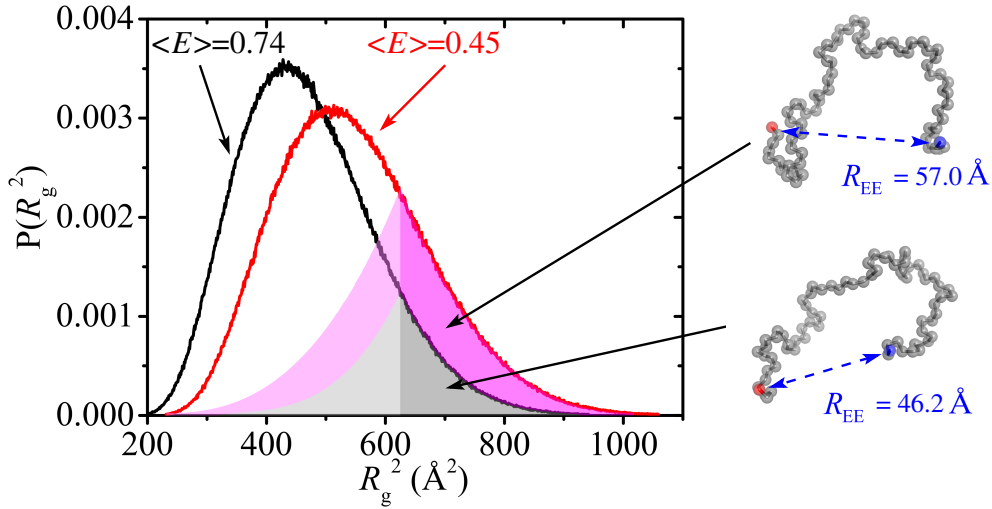


FIG. 7: A hypothetical resolution of the Protein L smFRET-SAXS puzzle. The two distributions depicted by the black and red curves are from Fig. 4d, for $\langle E \rangle = 0.74$ and $\langle E \rangle = 0.45$, respectively. For $R_g^2 \geq 625 \text{ \AA}^2$, area shaded in pink is under the $\langle E \rangle = 0.45$ (red) distribution but above the $\langle E \rangle = 0.74$ (black) distribution, whereas area shaded in grey is under the $\langle E \rangle = 0.74$ (black) distribution. The $R_g^2 < 625 \text{ \AA}^2$ areas that are in lighter shades are mirror reflections of the corresponding $R_g^2 \geq 625 \text{ \AA}^2$ areas with respect to $R_g^2 = 625 \text{ \AA}^2$. The sumtotal of the pink plus grey area represents a hypothetical ensemble with $\langle E \rangle \approx 0.45$ and root-mean-square $R_g = 25 \text{ \AA}$, whereas the grey area represent a hypothetical ensemble with $\langle E \rangle \approx 0.74$ but nonetheless the same root-mean-square $R_g = 25 \text{ \AA}$. Shown on the right are example conformations in these restricted ensembles, as marked by the arrows. Both conformations have $R_g^2 = 700 \text{ \AA}^2$ ($R_g = 26.5 \text{ \AA}$), but their different R_{EE} values entail different E values of ≈ 0.45 (top) and ≈ 0.74 (bottom). See text and Fig. 4 for further details.

numbers are important, nonetheless, for illustrating a key concept. If an explicit account of the atomic structure of the sidechains is used, for instance, the excluded volume effect would likely be slightly increased. Likewise, within the present C_α framework, if an excluded-volume repulsion length $R_{\text{hc}} = 5 \text{ \AA}$ is adopted instead of the present $R_{\text{hc}} = 4 \text{ \AA}$, the R_g distribution would shift upward by $\approx 2\text{--}3 \text{ \AA}$ [21]. In that case, the fractions of $P(R_g^2|E)$ and $P(R_g^2|\langle E \rangle)$ with $R_g^2 \geq 625 \text{ \AA}^2$ would increase, meaning that restrictive effects less severe than those estimated above would be sufficient for sequence-specific, denaturant-dependent conformational heterogeneity to resolve the smFRET-SAXS puzzle.

Concluding remarks. We deem this scenario for Protein L viable pending further experiment because natural proteins are heteropolymers, not homopolymers. Their amino acid sequences encode for heterogeneous intrachain interactions, especially under strongly folding (low or zero denaturant) conditions, which logically can only lead to

heterogeneous conformational ensembles even when the chains are disordered. The question is not whether heterogeneity exists but the degree of heterogeneity and its impact. Such heterogeneity is observable by NMR [72], not only for proteins such as BBL that do not fold cooperatively [73], but also for two-state folders (as defined by equality of van't Hoff and calorimetric enthalpies of unfolding, and chevron plots with linear folding and unfolding arms [24, 74]) such as cytochrome c [75]. The biophysics is readily understood theoretically [76, 77]. From a mathematical standpoint, it is definitely possible, as we envisioned above, for heterogeneous conformational ensembles that are distinct from random coils or SAWs to have overall random-coil or SAW dimensions nonetheless, as has been demonstrated by hypothetical explicit-chain ensembles constructed to embody such properties [78, 79]. The scenario we suggested for resolving the smFRET-SAXS discrepancy for Protein L posits an increased population of transient loop-like disordered conformations with the two chain termini close to each other under native conditions. Is this feasible? Of relevance to this question is the experimental finding that conformations with enhanced populations of nonlocal contacts are involved in the folding kinetics of adenylate kinase [80–82]. Conformations with similar properties have also been suggested by theory to be favored along folding transition paths [28]. Recently, a disordered conformational state with such properties was identified for the protein drkN SH3 as well, though in this case it is induced by high rather than by low denaturant [18]. All in all, it is clear from the above considerations that denaturant-dependent heterogeneity in disordered protein conformational ensembles is expected in general. To what degree and in what manner it may account for the smFRET-SAXS discrepancy will have to be ascertained by further experiment.

Supporting Material

One supporting figure is attached to the end of this document.

Author Contributions

J.S. and H.S.C. designed the research. J.S., G.-N.G. and H.S.C. performed the research. J.S., G.-N.G., C.C.G. and H.S.C. analyzed the data. T.S. contributed computational tools. J.S. and H.S.C. wrote the paper.

Acknowledgments

H.S.C. thanks Osman Bilsel and Elisha Haas for helpful discussions during Protein Folding Consortium workshops sponsored by the National Science Foundation (US). J.S. gratefully acknowledges support from the National Natural Science Foundation of China (Grant No. 21674055) and the Open Research Fund of State Key Laboratory of Polymer Physics and Chemistry, Changchun Institute of Applied Chemistry, Chinese Academy of Sci-

ences (Grant No. 201613). G.-N.G. was supported by an Ontario Graduate Scholarship. Support for this work was also provided by Natural Science and Engineering Research Council of Canada Discovery Grant RGPIN 342295-12. to C.C.G., Canadian Institutes of Health Research Operating Grant No. MOP-84281 to H.S.C., and generous allotments of computational resources from SciNet of Compute/Calcul Canada.

- [1] Haran, G. 2012 How, when and why protein collapse: The relation to folding. *Curr. Opin. Struct. Biol.* 22:14–20.
- [2] Schuler, B., and H. Hofmann. 2013. Single-molecule spectroscopy of protein folding dynamics—expanding scope and timescales. *Curr. Opin. Struct. Biol.* 23:36–47.
- [3] Gelman, H., and M. Gruebele. 2014. Fast protein folding kinetics. *Q. Rev. Biophys.* 47:95–142.
- [4] Juette, M. F., D. S. Terry, M. R. Wasserman, Z. Zhou, R. B. Altman, Q. Zheng, and S. C. Blanchard. 2014. The bright future of single-molecule fluorescence imaging. *Curr. Opin. Struct. Biol.* 20:103–111.
- [5] Elbaum-Garfinkle, S., G. Cobb, J. T. Compton, X.-H. Li, and E. Rhoades. 2014. Tau mutants bind tubulin heterodimers with enhanced affinity. *Proc. Natl. Acad. Sci. USA* 111:6311–6316.
- [6] Banerjee, P. R., and A. A. Deniz. 2014. Shedding light on protein folding landscapes by single-molecule fluorescence. *Chem. Soc. Rev.* 43:1172–1188.
- [7] König, K., A. Zarrine-Afsar, M. Aznauryan, A. Soranno, B. Wunderlich, F. Dingfelder, J. C. Stüber, A. Plückthun, D. Nettels, and B. Schuler. 2015. Single-molecule spectroscopy of protein conformational dynamics in live eukaryotic cells. *Nature Methods* 12:773–779.
- [8] Melo, A. M., J. Coraor, G. Alpha-Cobb, S. Elbaum-Garfinkle, A. Nath, and E. Rhoades. 2016. A functional role for intrinsic disorder in the tau-tubulin complex. *Proc. Natl. Acad. Sci. USA* 113:14336–14341.
- [9] Schuler, B., A. Soranno, H. Hofmann, and D. Nettels. 2016. Single-molecule FRET spectroscopy and the polymer physics of unfolded and intrinsically disordered proteins. *Annu. Rev. Biophys.* 45:207–231.
- [10] Uversky, V. N., C. J. Oldfield, and A. K. Dunker. 2008. Intrinsically disordered proteins in human diseases: Introducing the D² concept. *Annu. Rev. Biophys.* 37:215–246.
- [11] Tompa, P. 2012. Intrinsically disordered proteins: A 10-year recap. *Trends Biochem. Sci.* 37:509–516.
- [12] Forman-Kay, J. D., and T. Mittag. 2013. From sequence and forces to structure, function, and evolution of intrinsically disordered proteins. *Structure* 21:1492–1499.

- [13] Liu, Z., and Y. Huang. 2014. Advantages of proteins being disordered. *Protein Sci.* 23:539–550.
- [14] Chen, T., J. Song, and H. S. Chan. 2015. Theoretical perspectives on nonnative interactions and intrinsic disorder in protein folding and binding. *Curr. Opin. Struct. Biol.* 30:32–42.
- [15] Das, R. K., K. M. Ruff, and R. V. Pappu. 2015. Relating sequence encoded information to form and function of intrinsically disordered proteins. *Curr. Opin. Struct. Biol.* 32:102–112.
- [16] Sherman, E., and G. Haran. 2006. Coil-globule transition in the denatured state of a small protein. *Proc. Natl. Acad. Sci. USA* 103:11539–11543.
- [17] Merchant, K. A., R. B. Best, J. M. Louis, I. V. Gopich, and W. A. Eaton. 2007. Characterizing the unfolded states of proteins using single-molecule FRET spectroscopy and molecular simulations. *Proc. Natl. Acad. Sci. USA* 104:1528–1533.
- [18] Mazouchi, A., Z. Zhang, A. Bahram, G.-N. Gomes, H. Lin, J. Song, H. S. Chan, J. D. Forman-Kay, and C. C. Grdinaru. 2016. Conformations of a metastable SH3 domain characterized by smFRET and an excluded-volume polymer model. *Biophys. J.* 110:1510–1522.
- [19] Müller-Späth, S., A. Soranno, V. Hirschfeld, H. Hofmann, S. Rüegger, L. Reymond, D. Netters, and B. Schuler. 2010. Charge interactions can dominate the dimensions of intrinsically disordered proteins. *Proc Natl Acad Sci USA* 107:14609–14614.
- [20] Liu, B., D. Chia, V. Csizmok, P. Farber, J. D. Forman-Kay, and C. C. Grdinaru. 2014. The effect of intrachain electrostatic repulsion on conformational disorder and dynamics of the Sic1 protein. *J. Phys. Chem. B* 118:4088–4097.
- [21] Song, J., G.-N. Gomes, C. C. Grdinaru, and H. S. Chan. 2015. An adequate account of excluded volume is necessary to infer compactness and asphericity of disordered proteins by Förster resonance energy transfer. *J. Phys. Chem. B* 119:15191–15202.
- [22] Huang, F., L. Ying, and A. R. Fersht. 2009. Direct observation of barrier-limited folding of BBL by single-molecule fluorescence resonance energy transfer. *Proc. Natl. Acad. Sci. USA* 106:16239–16244.
- [23] Liu, J., L. A. Campos, M. Cerminara, X. Wang, R. Ramanathan, D. S. English, and V. Muñoz. 2012. Exploring one-state downhill protein folding in single molecules. *Proc. Natl. Acad. Sci. USA* 109:179–184.
- [24] Chan, H. S., Z. Zhang, S. Wallin, and Z. Liu. 2011. Cooperativity, local-nonlocal coupling, and nonnative interactions: Principles of protein folding from coarse-grained Models. *Annu. Rev. Phys. Chem.* 62:301–326.
- [25] Skinner, J. J., W. Yu, E. K. Gichana, M. C. Baxa, J. Hinshaw, K. F. Freed, and T. R. Sosnick. 2014. Benchmarking all-atom simulations using hydrogen exchange. *Proc. Natl. Acad. Sci. USA* 111:15975–15980.
- [26] Li, M., and Z. Liu. 2016. Dimensions, energetics, and denaturant effects of the protein unstructured state. *Protein Sci.* 25:734–747.

- [27] Chung, H. S., and W. A. Eaton. 2013. Single-molecule fluorescence probes dynamics of barrier crossing. *Nature* 502:685–688.
- [28] Zhang, Z., and H. S. Chan. 2012. Transition paths, diffusive processes, and preequilibria of protein folding. *Proc. Natl. Acad. Sci. USA* 109:20919–20924.
- [29] Borg, M., T. Mittag, T. Pawson, M. Tyers, J. D. Forman-Kay, and H. S. Chan. 2007. Poly-electrostatic interactions of disordered ligands suggest a physical basis for ultrasensitivity. *Proc. Natl. Acad. Sci. USA* 104:9650–9655.
- [30] Mittag, T., J. Marsh, A. Grishaev, S. Orlicky, H. Lin, F. Sicheri, M. Tyers, and J. D. Forman-Kay. 2010. Structure/function implications in a dynamic complex of the intrinsically disordered Sic1 with the Cdc4 subunit of an SCF ubiquitin ligase. *Structure* 18:494–506.
- [31] Fuxreiter, M., and P. Tompa. 2012. Fuzzy complexes: a more stochastic view of protein function. *Adv. Exp. Med. Biol.* 725:1–14.
- [32] Csizmok, V., S. Orlicky, J. Cheng, J. Song, A. Bah, N. Delgoshiae, H. Lin, T. Mittag, F. Sicheri, H. S. Chan, M. Tyers, and J. D. Forman-Kay. 2017. An allosteric conduit facilitates dynamic multisite substrate recognition by the SCF^{Cdc4} ubiquitin ligase. *Nat. Comm.* 8:13943.
- [33] Chong, P. A., and J. D. Forman-Kay. 2016. Liquid-liquid phase separation in cellular signaling systems *Curr. Opin. Struct. Biol.* 41:180–186.
- [34] Das, R. K., and R. V. Pappu. 2013. Conformations of intrinsically disordered proteins are influenced by linear sequence distribution of oppositely charged residues. *Proc. Natl. Acad. Sci. USA* 110:13392–13397.
- [35] Sawle, L., and K. Ghosh. 2015. A theoretical method to compute sequence dependent configurational properties in charged polymers and proteins. *J. Chem. Phys.* 143:085101.
- [36] Lin, Y.-H., J. D. Forman-Kay, and H. S. Chan. 2016. Sequence-specific polyampholyte phase separation in membraneless organelles. *Phys. Rev. Lett.* 117:178101.
- [37] Lin, Y.-H., and H. S. Chan. 2017. Phase separation and single-chain compactness of charged disordered proteins are strongly correlated. *Biophys. J.*, accepted, available online (<http://dx.doi.org/10.1016/j.bpj.2017.04.021>).
- [38] Ziv, G., and G. Haran. 2009. Protein folding, protein collapse, and Tanford’s transfer model: Lessons from single-molecule FRET. *J. Am. Chem. Soc.* 131:2942–2947.
- [39] Hofmann, H., D. Nettels, and B. Schuler. 2013. Single-molecule spectroscopy of the unexpected collapse of an unfolded protein at low pH. *J. Chem. Phys.* 139:121930.
- [40] Möglich, A., K. Jorder, and T. Kiehhaber. 2006. End-to-end distance distributions and intrachain diffusion constants in unfolded polypeptide chains indicate intramolecular hydrogen bond formation. *Proc. Natl. Acad. Sci. USA* 103:12394–12399.
- [41] Yoo, T. Y., S. P. Meisburger, J. Hinshaw, L. Pollack, G. Haran, T. R. Sosnick, and K.

Plaxco. 2012. Small-angle x-ray scattering and single-molecule FRET spectroscopy produce highly divergent views of the low-denaturant unfolded state. *J. Mol. Biol.* 418:226–236.

[42] Watkins, H. M., A. J. Simon, T. R. Sosnick, E. A. Lipman, R. P. Hjelm, and K. W. Plaxco. 2015. Random coil negative control reproduces the discrepancy between scattering and FRET measurements of denatured protein dimensions. *Proc. Natl. Acad. Sci. USA* 112:6631–6636.

[43] Holehouse, A. S., I. Perana, I. S. Carrico, O. Bilsel, D. P. Raleigh, and R. V. Pappu. 2017. Simulations and experiments provide a convergent view of protein unfolded states under folding conditions. 2017 Biophysical Society Meeting Abstracts. *Biophys. J. Supplement*, 315a, Abstract, 1550-Plat.

[44] Plaxco, K. W., I. S. Millet, D. J. Segel, S. Doniach, and D. Baker. 1999. Polypeptide chain collapse can occur concomitantly with the rate limiting step in protein folding. *Nature Struct. Biol.* 6:554–557.

[45] Jacob, J., B. Krantz, R. S. Dothager, P. Thiagarajan, and T. R. Sosnick. 2004. Early collapse is not an obligate step in protein folding. *J. Mol. Biol.* 338:369–382.

[46] O'Brien, E. P., G. Morrison, B. R. Brooks, and D. Thirumalai. 2009. How accurate are polymer models in the analysis of Förster resonance energy transfer experiments on proteins? *J. Chem. Phys.* 130:124903.

[47] Kellner, R., H. Hofmann, A. Barducci, B. Wunderlich, D. Nettels, D., and B. Schuler. 2014. Single-molecule spectroscopy reveals chaperone-mediated expansion of substrate protein. *Proc. Natl. Acad. Sci. USA* 111:13355–13360.

[48] Maity, H., and G. Reddy. 2016. Folding of Protein L with implications for collapse in the denatured state ensemble. *J. Am. Chem. Soc.* 138:2609–2616.

[49] Li, M., T. Sun, F. Jin, D. Yu, and Z. Liu. 2016. Dimension conversion and scaling of disordered protein chains. *Mol. Biosyst.* 12:2932–2940.

[50] Zheng, W., A. Borgia, K. Buholzer, A. Grishaev, B. Schuler, and R. B. Best. 2016. Probing the action of chemical denaturant on an intrinsically disordered protein by simulation and experiment. *J. Am. Chem. Soc.* 138:11702–11713.

[51] Borgia, A., W. Zheng, K. Buholzer, M. B. Borgia, A. Schuler, H. Hofmann, A. Soranno, D. Nettels, K. Gast, A. Grishaev, R. B. Best, and B. Schuler. 2016. Consistent view of polypeptide chain expansion in chemical denaturants from multiple experimental methods. *J. Am. Chem. Soc.* 138:11714–11726.

[52] Piana, S., J. L. Klepeis, and D. E. Shaw. 2014. Assessing the accuracy of physical models used in protein-folding simulations: Quantitative evidence from long molecular dynamics simulations. *Curr. Opin. Struct. Biol.* 24:98–105.

[53] Chen, T., and H. S. Chan. 2014. Effects of desolvation barriers and sidechains on local-nonlocal coupling and chevron behaviors in coarse-grained models of protein folding. *Phys.*

Chem. Chem. Phys. 16:6460–6479.

[54] Rauscher, S., V. Gapsys, M. J. Gajda, M. Zweckstetter, B. L. de Groot, and H. Grubmüller. 2015. Structural ensembles of intrinsically disordered proteins depend strongly on force field: A comparison to experiment. *J. Chem. Theor. Comput.* 11:5513–5524.

[55] Huang, J., S. Rauscher, G. Nawrocki, T. Ran, M. Feig, B. L. de Groot, H. Grubmüller, and A. D. MacKerell, Jr. 2017. CHARMM36m: An improved force field for folded and intrinsically disordered proteins. *Nat. Methods* 14:71–73.

[56] Best, R. B. 2017. Computational and theoretical advances in studies of intrinsically disordered proteins. *Curr. Opin. Struct. Biol.* 42:147–154.

[57] Levine, Z. A., and J.-E. Shea. 2017. Simulations of disordered proteins and systems with conformational heterogeneity. *Curr. Opin. Struct. Biol.* 43:95–103.

[58] Levitt, M. 1976. A simplified representation of protein conformations for rapid simulation of protein folding. *J. Mol. Biol.* 104:59–107.

[59] Metropolis, N., A. W. Rosenbluth, M. N. Rosenbluth, A. H. Teller, and E. Teller. 1953. Equation of state calculation by fast computing machines. *J. Chem. Phys.* 21:1087–1092.

[60] Song, J., S. C. Ng, P. Tompa, K. A. W. Lee, and H. S. Chan. 2013. Polycation- π interactions are a driving force for molecular recognition by an intrinsically disordered oncoprotein family. *PLoS Comput. Biol.* 9:e1003239.

[61] Verdier, P. H., W. H. Stockmayer. 1962. Monte Carlo calculations on dynamics of polymers in dilute solution. *J. Chem. Phys.* 36:227–235.

[62] Lal, M. 1969. Monte Carlo computer simulation of chain molecules. I. *Mol. Phys.* 17:57–64.

[63] McCarney, E. R., J. H. Werner, S. L. Bernstein, I. Ruczinski, D. E. Makarov, P. M. Goodwin, and K. W. Plaxco. 2005. Site-specific dimensions across a highly denatured protein; a single molecule study. *J. Mol. Biol.* 352:672–682.

[64] Kikhney, A. G., D. I. Svergun. 2015. A practical guide to small angle X-ray scattering (SAXS) of flexible and intrinsically disordered proteins. *FEBS Lett.* 589:2570–2577.

[65] Kohn, J. E., I. S. Millett, J. Jacob, B. Zagrovic, T. M. Dillon, N. Cingel, R. S. Dothager, S. Seifert, P. Thiagarajan, T. R. Sosnick, M. Z. Hasan, V. S. Pande, I. Ruczinski, S. Doniach, and K. W. Plaxco. 2004. Random-coil behavior and the dimensions of chemically unfolded proteins. *Proc. Natl. Acad. Sci. USA* 101:12491–12496.

[66] Inman, H. F., and E. L. Bradley Jr. 1989. The overlapping coefficient as a measure of agreement between probability distributions and point estimation of the overlap of two normal densities. *Comm. Stat. – Theory & Methods* 18:3851–3874.

[67] Hu, J., T. Chen, M. Wang, H. S. Chan, and Z. Zhang. 2017. A critical comparison of coarse-grained structure-based approaches and atomic models of protein folding. *Phys. Chem. Chem. Phys.*, accepted, available online (<http://dx.doi.org/10.1039/C7CP01532A>).

[68] Borgia, A., B. G. Wensley, A. Soranno, D. Nettels, M. B. Borgia, A. Hoffmann, S. H. Pfeil,

E. A. Lipman, J. Clarke, and B. Schuler. 2012. Localizing internal friction along the reaction coordinate of protein folding by combining ensemble and single-molecule fluorescence spectroscopy. *Nat. Comm.* 3:1195.

[69] Choy, W.-Y., and J. D. Forman-Kay. 2001. Calculation of ensembles of structures representing the unfolded state of an SH3 domain. *J. Mol. Biol.* 308:1011–1032.

[70] Marsh, J. A., and J. D. Forman-Kay. 2012. Ensemble modeling of protein disordered states: Experimental restraint contributions and validation. *Proteins* 80:556–572.

[71] Antonov, L. D., S. Ollsson, W. Boomsma, and T. Hamelryck. 2016. Bayesian inference of protein ensembles from SAXS data. *Phys. Chem. Chem. Phys.* 18:5832–5838.

[72] Baldwin, R. L. 1995. The nature of protein folding pathways: The classical versus the new view. *J. Biomol. NMR* 5:103–109.

[73] Sadqi, M., D. Fushman, and V. Muñoz. 2006. Atom-by-atom analysis of global downhill protein folding. *Nature* 442:317–321.

[74] Chan, H. S., S. Shimizu, and H. Kaya. 2004. Cooperativity principles in protein folding. *Methods Enzymol.* 380:350–379.

[75] Bai, Y., T. R. Sosnick, L. Mayne, and S. W. Englander. 1995. Protein folding intermediates: Native-state hydrogen exchange. *Science* 269:192–197.

[76] Kaya, H., and H. S. Chan. 2005. Explicit-chain model of native-state hydrogen exchange: Implications for event ordering and cooperativity in protein folding. *Proteins* 58:31–44.

[77] Knott, M., and H. S. Chan. 2006. Criteria for downhill protein folding: Calorimetry, chevron plot, kinetic relaxation, and single-molecule radius of gyration in chain models with subdued degrees of cooperativity. *Proteins* 65:373–391.

[78] Pappu, R. V., R. Srinivasan, and G. D. Rose. 2000. The Flory isolated-pair hypothesis is not valid for polypeptide chains: Implications for protein folding. *Proc. Natl. Acad. Sci. USA* 97:12565–12570.

[79] Fitzkee, N. C., and G. D. Rose. 2004. Reassessing random-coil statistics in unfolded proteins. *Proc. Natl. Acad. Sci. USA* 101:12497–12502.

[80] Orevi, T., E. B. Ishay, M. Pirchi, M. H. Jacob, D. Amir, and E. Haas. 2009. Early closure of a long loop in the refolding of adenylate kinase: A possible key role of non-local interactions in the initial folding steps. *J. Mol. Biol.* 385:1230–1242.

[81] Lemer, E., T. Orevi, E. B. Ishay, D. Amir, and E. Haas. 2014. Kinetics of fast changing intramolecular distance distributions obtained by combined analysis of FRET efficiency kinetics and time-resolved FRET equilibrium measurements. *Biophys. J.* 106:667–676.

[82] Orevi, T., G. Rahamin, D. Amir, S. Kathuria, O. Bilsel, C. R. Matthews, and E. Haas. 2016. Sequential closure of loop structures forms the folding nucleus during the refolding transition of the *Escherichia coli* adenylate kinase molecule. *Biochemistry* 55:79–91.

Supporting Figure

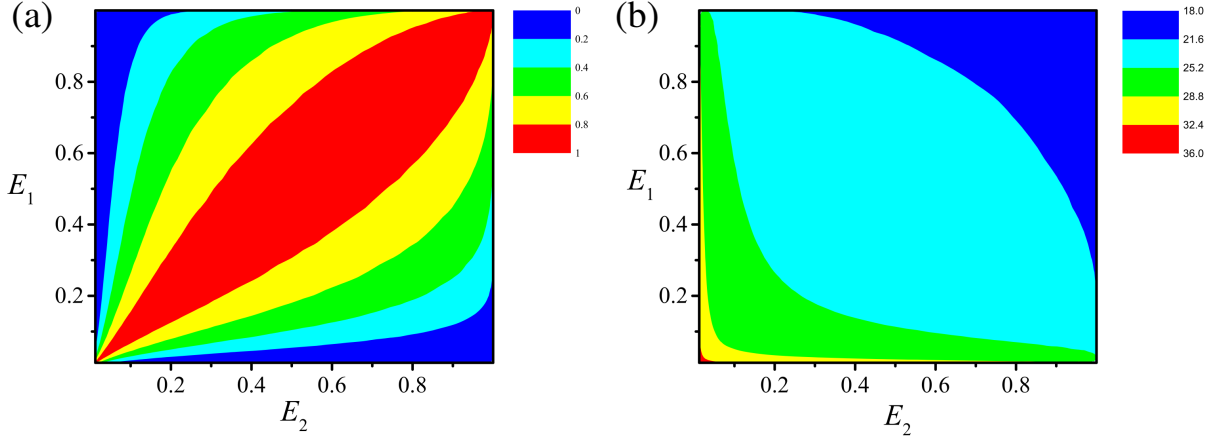


Figure S1.

Overlapping R_g^2 distributions for pairs of FRET efficiencies. Results shown are for $n = 75$ and $R_0 = 55$ Å. (a) Same data as Fig. 5 of the main text plotted in a different style. The color code here indicates range of values for the overlapping coefficient $OVL[P(R_g^2|E_1), P(R_g^2|E_2)]$. The fractional areas in red, yellow, green, cyan, and blue are, respectively, 0.311, 0.267, 0.193, 0.128, and 0.101. (b) Root-mean-squared radius of gyration averaged over the overlapping region of $P(R_g^2|E_1)$ and $P(R_g^2|E_2)$. The value represented by the color code is given by $\sqrt{\int dR_g^2 R_g^2 \{ \min[P(R_g^2|E_1), P(R_g^2|E_2)] \}}$. For instance, this quantity for the pair of distributions in Fig. 4c of the main text with $E_1 \approx 0.447$ and $E_2 \approx 0.745$ ($OVL = 0.747$) is equal to $\sqrt{503.6 \text{ \AA}^2} = 22.4$ Å. Note that this value is practically identical to the value of $\sqrt{505.1 \text{ \AA}^2} = 22.5$ Å for the root-mean-squared radius of gyration averaged over the overlap area in Fig. 4d of the main text for two broad E distributions with $OVL = 0.754$.